RESEARCH ARTICLE SUMMARY

PLANETARY SCIENCE

Cryovolcanism on Ceres

O. Ruesch,* T. Platz, P. Schenk, L. A. McFadden, J. C. Castillo-Rogez, L. C. Quick, S. Byrne, F. Preusker, D. P. O'Brien, N. Schmedemann, D. A. Williams, J.-Y. Li, M. T. Bland, H. Hiesinger, T. Kneissl, A. Neesemann, M. Schaefer, J. H. Pasckert, B. E. Schmidt, D. L. Buczkowski, M. V. Sykes, A. Nathues, T. Roatsch, M. Hoffmann, C. A. Raymond, C. T. Russell

INTRODUCTION: Classic volcanism prevalent on terrestrial planets and volatile-poor protoplanets, such as asteroid Vesta, is based on silicate chemistry and is often expressed by volcanic edifices (unless erased by impact bombardment). In ice-rich bodies with sufficiently warm interiors, cryovolcanism involving liquid brines can occur. Smooth plains on some icy satellites of the outer solar system have been suggested as possibly cryovolcanic in origin. However, evidence for cryovolcanic edifices has proven elusive. Ceres is a volatile-rich dwarf planet with an average equatorial surface temperature of ~160 K. Whether this small (~940 km diameter) body without tidal dissipation could sustain cryovolcanism has been an open question because the surface landforms and relation to internal activity were unknown.

RATIONALE: The Framing Camera onboard the Dawn spacecraft has observed >99% of Ceres' surface at a resolution of 35 m/pixel at visible wavelengths. This wide coverage and resolution were exploited for geologic mapping and age determination. Observations with a resolution of 135 m/pixel were obtained under several different viewing geometries. The stereo-photogrammetric method applied to this data set allowed the calculation of a digital terrain model, from which morphometry was investigated. The observations revealed a 4-km-high topographic relief, named Ahuna Mons, that is consistent with a cryovolcanic dome emplacement.

RESULTS: The ~17-km-wide and 4-km-high Ahuna Mons has a distinct size, shape, and morphology. Its summit topography is concave downward, and its flanks are at the angle of repose. The morphology is characterized by (i) troughs, ridges, and hummocky areas at the summit, indicating multiple phases of activity, such as extensional fracturing, and (ii) downslope lineations on the flanks, indicating rockfalls and accumulation of slope debris. These morphometric and morphologic observations are explained by the formation of a cryovolcanic dome, which is analogous to a high-viscosity silicic dome on terrestrial planets. Models indicate that extrusions of a highly viscous melt-bearing material can lead to the buildup of a brittle carapace at the summit, enclosing a ductile core. Partial fracturing and disintegration of the carapace generates slope debris, and relaxation of the dome's ductile core due to gravity shapes the topographic profile of the summit. Modeling of this final phase of dome relaxation and reproduction of the topographic profile requires an extruded material of high viscosity, which is consistent with the mountain's morphology. We constrained the age of the most recent activity on Ahuna Mons to be within the past 210 ± 30 million years.

ON OUR WEBSITE

Read the full article at http://dx.doi.org/10.1126/science.aaf4286

CONCLUSION: Cryovolcanic activity during the geologically recent past of Ceres constrains its thermal and chemical history. We propose that hydrated salts with low eutectic temperatures and low thermal conductivities enabled the presence of cryomagmatic liquids within Ceres. These salts are the product of global aqueous alteration, a key process for Ceres' evolution as recorded by the aqueously altered, secondary minerals observed on the surface. ■

The list of author affiliations is available in the full article online.
*Corresponding author. Email: ottaviano.ruesch@nasa.gov
Cite this article as O. Ruesch *et al.*, *Science* 353, aaf4286 (2016). DOI: 10.1126/science.aaf4286

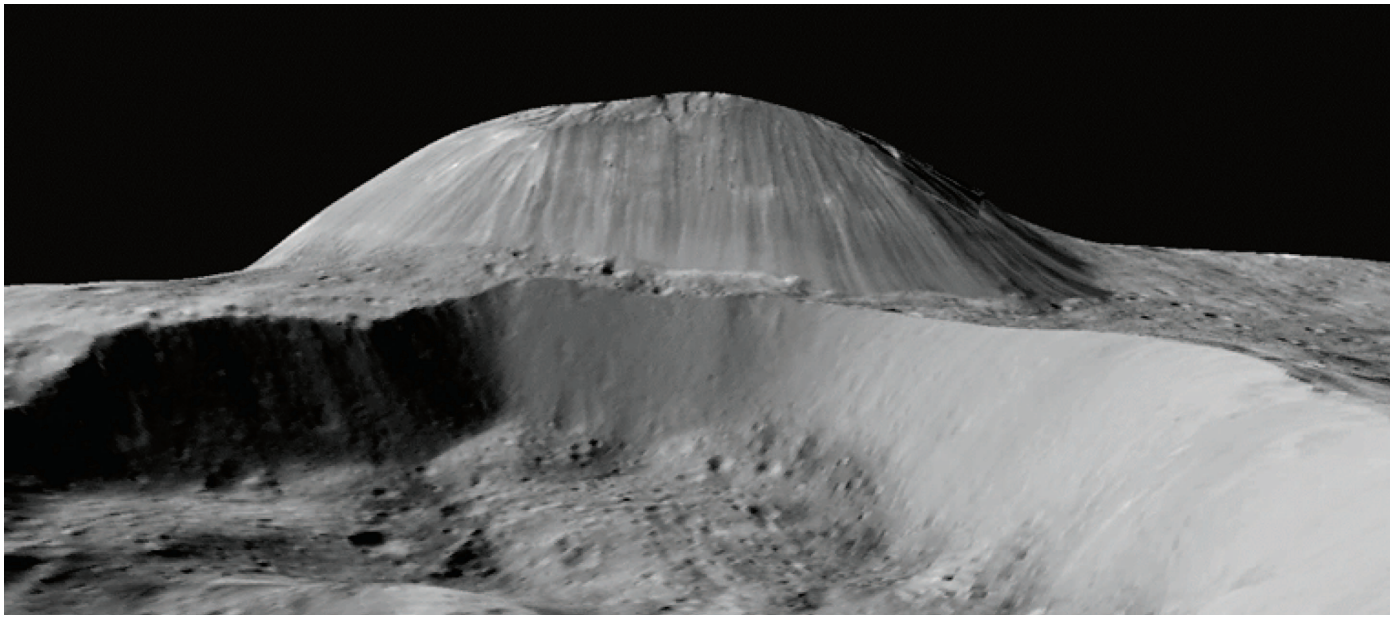

Perspective view of Ahuna Mons on Ceres from Dawn Framing Camera data (no vertical exaggeration). The mountain is 4 km high and 17 km wide in this south-looking view. Fracturing is observed on the mountain's top, whereas streaks from rockfalls dominate the flanks.

RESEARCH ARTICLE

PLANETARY SCIENCE

Cryovolcanism on Ceres

O. Ruesch,[1]* T. Platz,[2] P. Schenk,[3] L. A. McFadden,[4] J. C. Castillo-Rogez,[5] L. C. Quick,[6] S. Byrne,[7] F. Preusker,[8] D. P. O'Brien,[6] N. Schmedemann,[9] D. A. Williams,[10] J.-Y. Li,[6] M. T. Bland,[11] H. Hiesinger,[12] T. Kneissl,[9] A. Neesemann,[9] M. Schaefer,[2] J. H. Pasckert,[12] B. E. Schmidt,[13] D. L. Buczkowski,[14] M. V. Sykes,[6] A. Nathues,[2] T. Roatsch,[8] M. Hoffmann,[2] C. A. Raymond,[5] C. T. Russell[15]

Volcanic edifices are abundant on rocky bodies of the inner solar system. In the cold outer solar system, volcanism can occur on solid bodies with a water-ice shell, but derived cryovolcanic constructs have proved elusive. We report the discovery, using Dawn Framing Camera images, of a landform on dwarf planet Ceres that we argue represents a viscous cryovolcanic dome. Parent material of the cryomagma is a mixture of secondary minerals, including salts and water ice. Absolute model ages from impact craters reveal that extrusion of the dome has occurred recently. Ceres' evolution must have been able to sustain recent interior activity and associated surface expressions. We propose salts with low eutectic temperatures and thermal conductivities as key drivers for Ceres' long-term internal evolution.

The nature of Ceres' landforms and their relation to potential interior activity were unknown until the arrival of NASA's Dawn spacecraft in March 2015 (*1*). Ceres has a silicate interior overlain by an outer layer rich in volatiles (*1*, *2*) and a regolith bearing carbonates and phyllosilicates (*3*). Annual average surface temperature at the equator is ~160 K (*4*). Volcanism involving melt composed mostly of brines and other volatiles has been suggested on a theoretical basis for that type of body (*5*), differing from that of silicate volcanism on terrestrial planets. Some icy satellites of the outer solar system have surfaces dominated by plains of probable cryovolcanic origin (*6*–*8*). Evidence for cryovolcanic extrusive edifices such as volcanoes or domes remains elusive, however (*9*–*11*). The Dawn Framing Camera (FC) (*12*) acquired multiband visible images at a resolution of 35 m/pixel, covering >99% of Ceres' surface. A digital terrain model was calculated from stereophotogrammetry at a resolution of 205 m/pixel (Materials and methods). An isolated mountain, named Ahuna Mons [centered at 10.3°S, 316.2°E, (*1*)], has been identified (Fig. 1). Topographic rises broader than Ahuna Mons are common on Ceres (*13*), but the mountain is distinct in its size, shape, and morphology.

[1]NASA Goddard Space Flight Center/Universities Space Research Association (USRA), Greenbelt, MD, USA. [2]Max Planck Institute for Solar System Research, Göttingen, Germany. [3]Lunar and Planetary Science Institute, Houston, TX, USA. [4]NASA Goddard Space Flight Center, Greenbelt, MD, USA. [5]Jet Propulsion Laboratory, California Institute of Technology, Pasadena, CA, USA. [6]Planetary Science Institute, Tucson, AZ, USA. [7]Lunar and Planetary Laboratory, University of Arizona, Tucson, AZ, USA. [8]German Aerospace Center (DLR), Berlin, Germany. [9]Institute of Geosciences, Freie Universität Berlin, Berlin, Germany. [10]School of Earth and Space Exploration, Arizona State University, Tempe, AZ, USA. [11]U.S. Geological Survey, Astrogeology Science Center, Flagstaff, AZ, USA. [12]Institut für Planetologie, Westfälische Wilhelms-Universität, Münster, Germany. [13]Georgia Institute of Technology, Atlanta, GA, USA. [14]Johns Hopkins Applied Physics Laboratory, Laurel, MD, USA. [15]Department of Earth and Space Sciences, University of California, Los Angeles, CA, USA.
*Corresponding author. Email: ottaviano.ruesch@nasa.gov

Regional context

The photogeologic map presented in Fig. 1D represents a discretization of the surface geology into three-dimensional units formed by distinct events and processes. Map units were defined and characterized through visual investigation of surface texture and morphology, quantitative investigation of albedo and topography, and determination of ages on the basis of relative stratigraphy and crater size-frequency distributions (CSFDs). The area close to Ahuna Mons is moderately cratered (*14*) and is dissected by troughs (in the "cratered unit"; Fig. 1D, brown). Topographically, it presents two positive reliefs (a tholus and a mons) and two negative reliefs (crater A and crater B). The tholus is a ~30-km-wide topographic bulge (Fig. 1D), with an irregular base rising ~2 km above the surroundings. A ~40-km-diameter impact crater (Fig. 1D, crater A) cuts the southern part of the tholus and is thus younger. The northern section of this crater floor is filled with material displaying two parallel ridges a few kilometers long. The origin of the fill could be ejecta from adjacent impacts or other material related to the continuing development of the tholus after the formation of crater A. North of the tholus is a 17-km-diameter and moderately degraded impact crater (Fig. 1D, crater B) that may have contributed to the fracturing of the subsurface near the tholus. Ahuna Mons is located southeast of the 17-km-diameter impact crater and dominates the northern flank of the tholus (Fig. 2B). The basal planform of Ahuna Mons is elliptical (21 by 13 km), and its topographic profile is concave downward (Fig. 2C) with an elevation of ~4 km, leading to an aspect ratio (height/basal average diameter) of ~0.24. The mountain is surrounded by a smooth-textured unit (Fig. 1D, "smooth unit," blue), which is less cratered than adjacent material. The smooth unit may represent ejecta material from the 17-km-diameter crater or could be associated with the formation of the mountain.

Morphology of Ahuna Mons

Ahuna Mons consists of steep (30° to 40°) flanks of talus (slope debris) material (Fig. 3C, "talus unit," green) and a slightly (~300 m deep) topographically depressed (Fig. 3B) summit unit (Fig. 3C, "summit unit," pink). Little accumulated debris at the base of the talus unit leaves a dramatically sharp contact between the talus and the surrounding smooth unit (Fig. 3A). The contact to the northwest is characterized by a curvilinear relief of smooth unit material, less than 50 m high, and oriented parallel to the mountain's flank. It could represent uplifted and tilted material due to a subsurface intrusion or a compressional ridge formed by the edifice sagging and spreading (*15*). Downslope lineations are evident on the flanks and are likely caused by gravitationally driven rock falls (Fig. 3A). They are associated with photometrical and spectral variations (Materials and methods) (Fig. 4). The summit of Ahuna Mons is not covered by debris and displays a variety of structures. Troughs and ridges are present, with an average length of 1 km, 1 km maximum width, and variable orientation (Fig. 3C). They are plausibly formed by extensional forces in a brittle layer. Summit areas lacking troughs and ridges appear hummocky, with depressions smaller than 1 km (Fig. 3C, "pit") and hills less than 500 m in diameter (Fig. 3C, "knob"). Depressions can be the product of both exogenic (impacts) and endogenic (explosion or sublimation) events. Small hills could represent tilted blocks of a disrupted brittle layer or extrusion of new material penetrating the layer.

Age of Ahuna Mons

The ages of the smooth unit and the 17-km crater unit (crater B) sets the oldest possible formation age of Ahuna Mons because these units predate or are contemporaneous with the mountain formation. We measured CSFDs on these units and applied two different chronology models to derive absolute model ages (*14*). Measurements of CSFDs were performed within a geographic information system (GIS) environment (Esri's ArcGIS) by using the CraterTools add-in (*16*). The measurements were carried out on the basis of High Altitude Mapping Orbit FC clear-filter image, and the resulting CSFDs were analyzed in their cumulative form with the software CraterStats (*17*). One chronology model scales the lunar crater production and chronology functions to impact conditions on Ceres. This approach assumes for Ceres the same size-distribution of projectiles and the same time-dependence of the projectile flux as observed on the Moon (*14*). The alternative model derives a production function from the observed and extrapolated object size-frequency distribution of the main asteroid belt and a chronology

function based on simulated collision rates in the main asteroid belt (*14*). We determined that the smooth unit and the 17-km crater unit are of similar age: 210 ± 30 million years and 160 ± 30 million years, respectively, using the Lunar Derived Model or 70 ± 20 million years and 70 ± 20 million years, respectively, using the Asteroid Derived Model (Fig. 5). Both ages indicate that Ahuna Mons formed in the geologically recent past. Downslope lineations occur on young steep slopes of bodies where the regolith is immature (*18*). On asteroid Vesta, where the regolith develops at a lower rate than on Ceres (*19*), downslope lineations are erased on surfaces older than 200 to 400 million years (*18*). Thus, these features on the flanks of Ahuna Mons are consistent with the young age inferred from crater size-frequency distributions. Although the compositional or surface physical variation represented by the lineations is not discernible in the current data set, it is typical of recently exposed surfaces on Ceres, such as morphologically fresh impact craters. Additionally, a recent emplacement explains the sharp contact between the smooth and talus units because with time and impact bombardment on the flank, the contact would become increasingly diffuse and gradated.

Formation mechanisms

The morphological units of the region near Ahuna Mons and their stratigraphic relations (Fig. 1D) are indicative of a geological construct. There is no evidence for compressional tectonism nor erosional features such as mesas. Likewise, surface upwarping by diapirism (buoyantly rising material), without piercing the surface, is excluded as a formation mechanism because it requires a thin elastic crust, for which no evidence has been found on Ceres (Materials and methods). Instead, the aspect ratio of Ahuna Mons points to a dome formed mostly through extrusion (*20*). The variety of morphologies characterizing the summit unit and the nonsystematic orientation of troughs and ridges are presumably manifestations of multiple dome-forming phases. In contrast, solid-state extrusions on Earth, represented by salt plugs, are formed in a single phase of continuous, slow influx of plug material (*21*). The ductile plug material develops characteristic surface structures (such as folds and salt glaciers) (*22*) not observed on the summit unit.

Multiple phases of fracturing and possibly small-scale extrusions (hills) recorded on the summit indicate the composite nature of Ahuna Mons. This characteristic is analogous to high-viscosity volcanic domes on Earth that grow through a sequence of events such as extensional fracturing and extrusion of lobes (*23*–*25*). The summit unit thus represents a brittle dome carapace, formed by cooling of the outermost region of a ductile core. The fracturing of the carapace leads to its partial disintegration and production of boulders and smaller debris (*26*). Through mass wasting, these unconsolidated materials accumulate into talus. Thus, the talus formation is genetically part of the dome emplacement process and is not the result of erosion by impacts.

The aspect ratio, talus collar, and summit morphologies are indicative of an extrusive volcanic dome, similar to those found on Earth and the Moon (Fig. 6) (*20*, *23*, *27*). The aspect ratio and absence of flow morphologies suggest that the ductile core has a relatively high viscosity (*23*), as discussed in detail below. Although the materials compositions are different, the number of geomorphological analogies between Ahuna Mons and edifices on Earth suggests that other key properties (such as viscosity) between different planetary bodies are similar and lead to comparable geomorphologic features.

Modeling of topographic profile

We verify that the observed topographic profile of the Ahuna Mons is similar to that of a viscous volcanic dome, as suggested by its aspect ratio. For this purpose, we assume that the profile of a static dome reflects the mechanical equilibrium between a brittle carapace enclosing a pressurized ductile material (*28*). A carapace thickness of several hundred meters, as inferred from the summit troughs (Materials and methods), reproduce the concave downward profile of the Ahuna Mons summit (Fig. 7A), indicating that high-viscosity dome development is a viable mechanism for the formation of the mountain. The farthest section (lower flank) of the profile is found to be of constant slope (Fig. 7, A and B, black line), as expected for talus (*28*).

For estimates of rheological properties of the material, we turn to a dynamic model that describes the lateral spreading of a dome under the effect of gravity (*29*, *30*). The volume of the dome, calculated from the static model profile, is considered constant, and thus the dynamic model simulates only the final phase of dome evolution. Initial apparent dynamic viscosity of the dome material is set as a free parameter and is allowed to increase with time because of cooling and will halt the spreading. Modeling

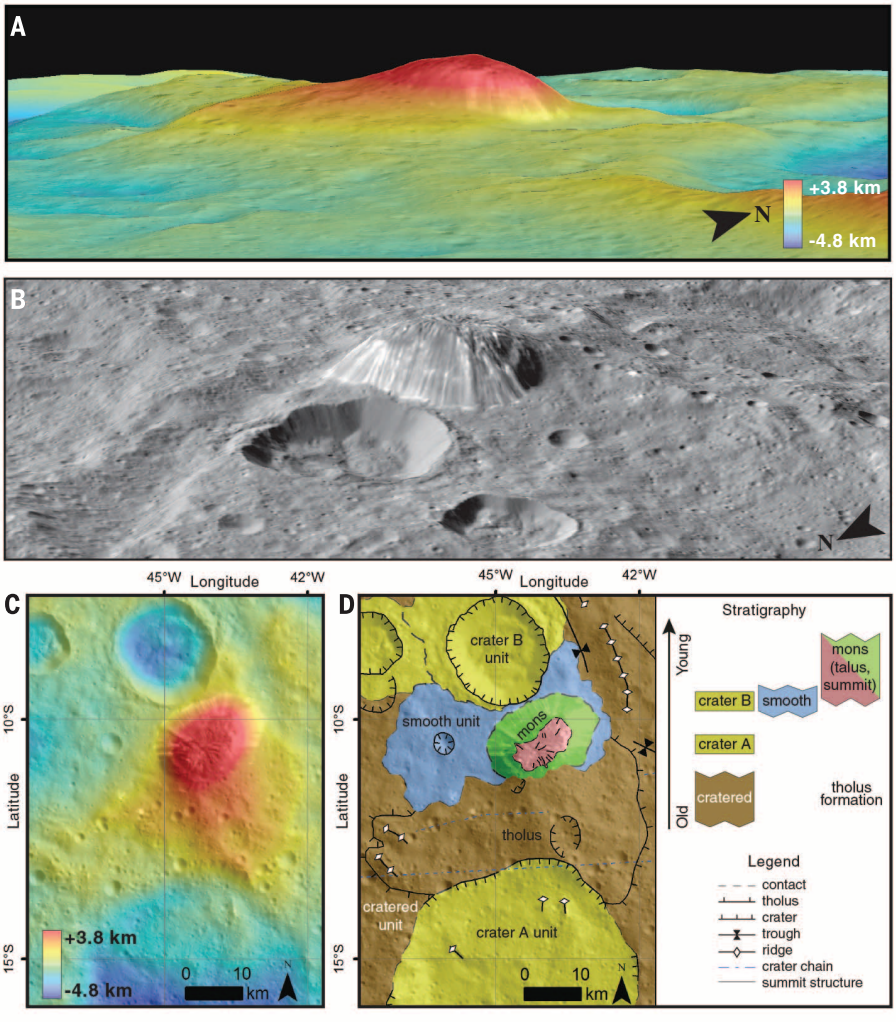

Fig. 1. Geologic context of Ahuna Mons. (**A**) Perspective view of the Ahuna Mons region derived from FC images and digital terrain model (Materials and methods). The view is looking west, and the scene is ~70 km wide in the foreground. (**B**) Perspective view of Ahuna Mons region looking southeast. Scene is ~70 km wide in the foreground. (**C**) Cylindrical projection of the FC image (FC21A0039691) and digital terrain model shown in (A). (**D**) Geologic map of the region shown in (C), with colors corresponding to units shown in the stratigraphic column.

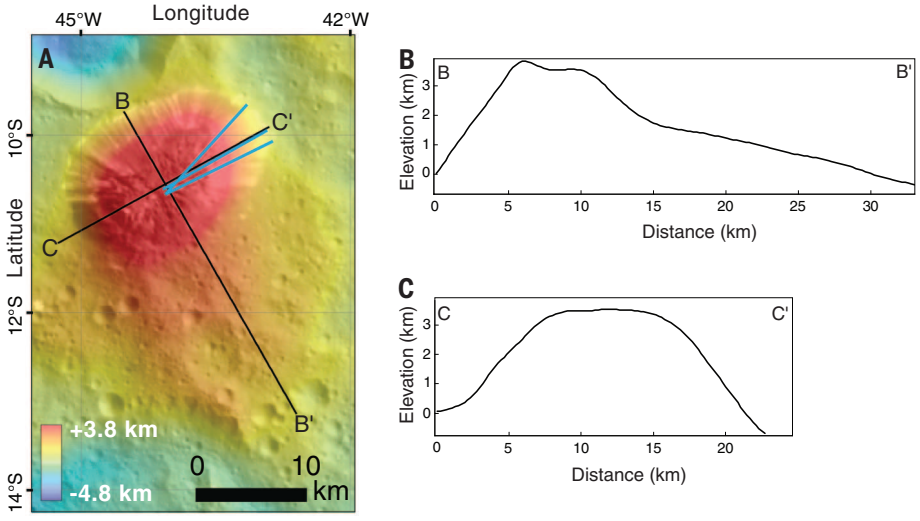

Fig. 2. Topography of Ahuna Mons and adjacent bulge. (**A**) Color-coded digital terrain model. The location of profile B–B' and C–C' are indicated with black lines and are shown in (B) and (C). The half cross sections shown in blue are averaged and shown in Fig. 7B. (**B**) Topographic profile across the tholus and mons. The profile of Ahuna Mons is asymmetrical. (**C**) Topographic profile across the Ahuna Mons. The profile is relatively symmetrical. Elevations are relative to an ellipsoid (482 by 482 by 446 km).

dome topography in this way (Fig. 7B) allows us to explore the range of initial apparent viscosity and the relaxation (spreading) time that reproduce the topography of Ahuna Mons (Materials and methods). The duration of spreading is constrained by a range of cooling time scales of the dome. The time scale based on radiative cooling is 4×10^2 years, whereas conductive cooling requires 3×10^5 years (Materials and methods). The size and shape of the Ahuna Mons profile can be reproduced within the fast cooling time scale with an initial apparent viscosity of 4×10^{15} Pa s, or within the slow cooling time with an initial apparent viscosity of 3×10^{18} Pa s (Fig. 7B). The viscosities are referred to as apparent because they represent the viscosity of the entire dome at the onset of spreading, including the ductile core and brittle carapace, which is known to mechanically limit the spreading of the dome. The effect of the carapace has been characterized as an increase in the apparent viscosity of the entire dome of approximately four orders of magnitude (*31*). This leads to initial actual dynamic viscosities ranging from 4×10^{11} to 3×10^{14} Pa s. The advance of the dome front is further reduced by the talus collar, and therefore, we consider this range as an upper estimate. This rheological evaluation confirms the highly viscous nature of the material inferred from morphology. Viscosities of terrestrial volcanic domes calculated from morphometry and detailed modeling of dome growth and evolution are up to 3×10^{12} Pa s, within the range estimated here (*32*).

Discussion

For the formation of Ahuna Mons, we thus propose a volcanic process involving ascent of cryomagma and extrusion onto the surface followed by dome development and spreading. Pathways for rising material were possibly provided by fractures produced by nearby impacts (Fig. 1D, crater B) and by the regional troughs (Fig. 1D). Second, large impacts on planetary bodies generate shock waves that can cause fracturing of the outermost layers at regions antipodal to impact structures (*33*). Ahuna Mons could be part of a broader, fractured antipodal region of Kerwan (10.9°S, 123.6°E), the largest preserved impact basin on Ceres with a diameter of ~280 km (*14*).

With the plausible initial viscosities presented above and Ceres composition revealed by the Dawn visible and near-infrared imaging spectrometer (*3*, *34*), a few characteristics of the cryomagma can be proposed. Ceres has warmer surface temperatures than those of icy satellites (*4*) but is of relatively small size and lacks tidal dissipation as a heat source. Temperatures were predicted to be as warm as 230 K starting at >50 km depth (*35*), conditions at which the homologous temperature of water ice is low. Our results imply a long-term heat source in the interior as well as the presence of low-eutectic temperature materials for the production of cryomagma (*5*). On the basis of mineralogical observations at the Occator crater (*34*), chloride salts may be present at depths within Ceres. The eutectic temperatures of chlorides are close to or lower than 230 K, hence enabling melt formation at ~50 km depth, or at shallower depths (*35*, *36*). The presence of a few percent of melt lead to a decrease in viscosity by >5 orders of magnitude compared with the solid parent material, and even more if the melt is connected (*37*). We propose that the parent material of the cryomagma may consist of chloride-rich brines, the potential melt phase; secondary minerals, such as carbonates and phyllosilicates (*3*); and water ice. Crucial information on the extruded material at a microscopic scale—compositional and textural characteristics at a sample scale—is missing, and despite chloride brines being frequent in terrestrial environments, relevant rheological data are lacking. As a consequence, we are unable to determine the melting behavior of the proposed parent material (for example, the percentage of melt upon extrusion), nor the proportions of the components in the resulting cryomagma, or the exact mechanism enabling its ascent and eruption. However, our understanding will improve with further determination of local-scale mineralogy and gravity measurements, as well as supporting experimental measurements. The presence of low-eutectic salts is consistent with a past phase of aqueous alteration of the rocky component at a global scale, as indicated by the surface mineralogy (*3*). This process was key for Ceres chemical and thermal evolution because the interaction enabled the leaching of alkali, alkaline-earth, and other soluble materials from the rock into fluids. The aqueous alteration allowed the fluid to become enriched with impurities, such as salts of low thermal conductivity, and radionuclides (^{40}K in particular)—hence, the displacement of the main long-term heat source from the core to the mantle (*38*) where cryomagma production occurred.

Although the broader and more degraded topographic rises on Ceres (*13*) are distinct from Ahuna Mons in several aspects, they might share a common formation process and imply that volcanic activity occurred over an extended period. Their different morphologies might be related to a change in the rheological properties of cryomagmas with time or during ascent, as proposed for lunar analogs (*27*). Ceres cryovolcanic activity and the composition of its cryomagma adds to the geological diversity of the solar system because they differ from volcanism of volatile-poor protoplanets. For example, on Vesta, volcanism based on igneous minerals was active only in the first tens of millions of years (*39*). The evolution of Ceres, dictated by its volatile-rich composition, resulted in the production of cryomagmatic liquids that enabled surface activity in geologically recent times.

Materials and methods

Description of digital terrain model method

The stereo-photogrammetric processing of Ceres Framing Camera images is based on a software suite described in (*40*–*44*). The stereo-photogrammetric processing is segmented into five steps: photogrammetric block adjustment, multi-image matching, surface point triangulation, digital terrain model (DTM) generation, and basemap generation (*42*). The cartography system is the International Astronomical Union system defined by the tiny crater Kait (*1*). The DTM used in this study is calculated with respect to an ellipsoid with a grid space of ~205 m/pixel. The height is given with an uncertainty of 14 m.

Discussion of diapirism as formation mechanism

The surface topography of an elastic layer resulting from an ascending spherical diapir was described by (*45*). With an elastic modulus of 1-10 GPa and Ceres' surface gravity of 0.28 m s^{-2} (*1*),

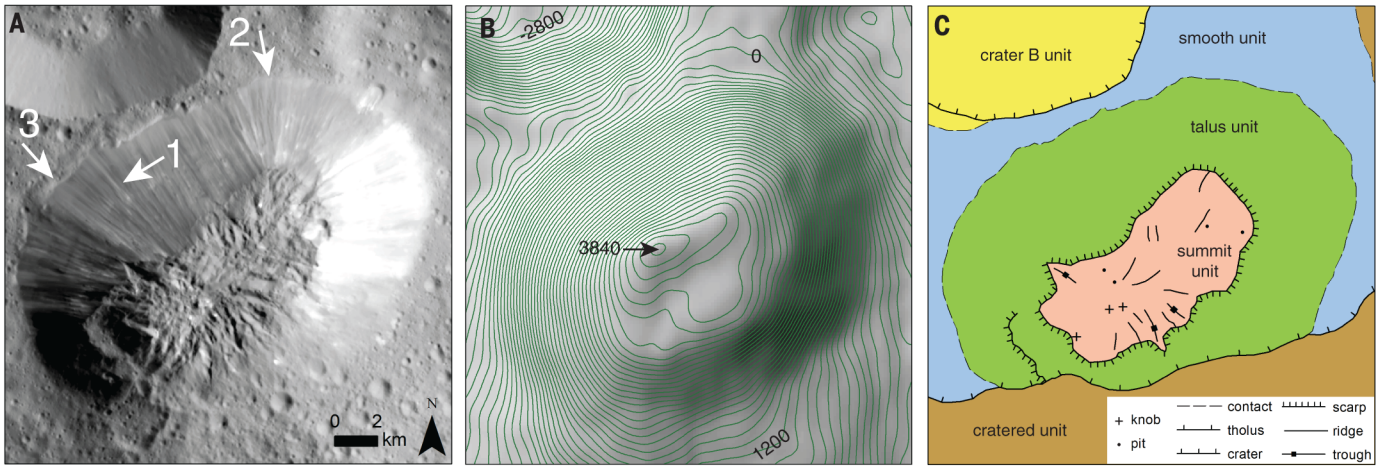

Fig. 3. Morphologies of Ahuna Mons. (**A**) FC image of the Ahuna Mons at a resolution of 35 m/pixel. Arrow 1 points to one of many brighter downslope lineations. Arrow 2 points to the sharp contact between smooth and talus units. Arrow 3 indicates where the smooth unit forms a relief extending along the contact with the talus unit. Cylindrical projection is centered at 10.3°S, 316.2°E. (**B**) Hill-shaded digital terrain model with superimposed 100 m contour lines. Key elevations are marked. Same location and projection as (A). (**C**) Close-up of the geologic map centered on Ahuna Mons. Same location and projection as (A).

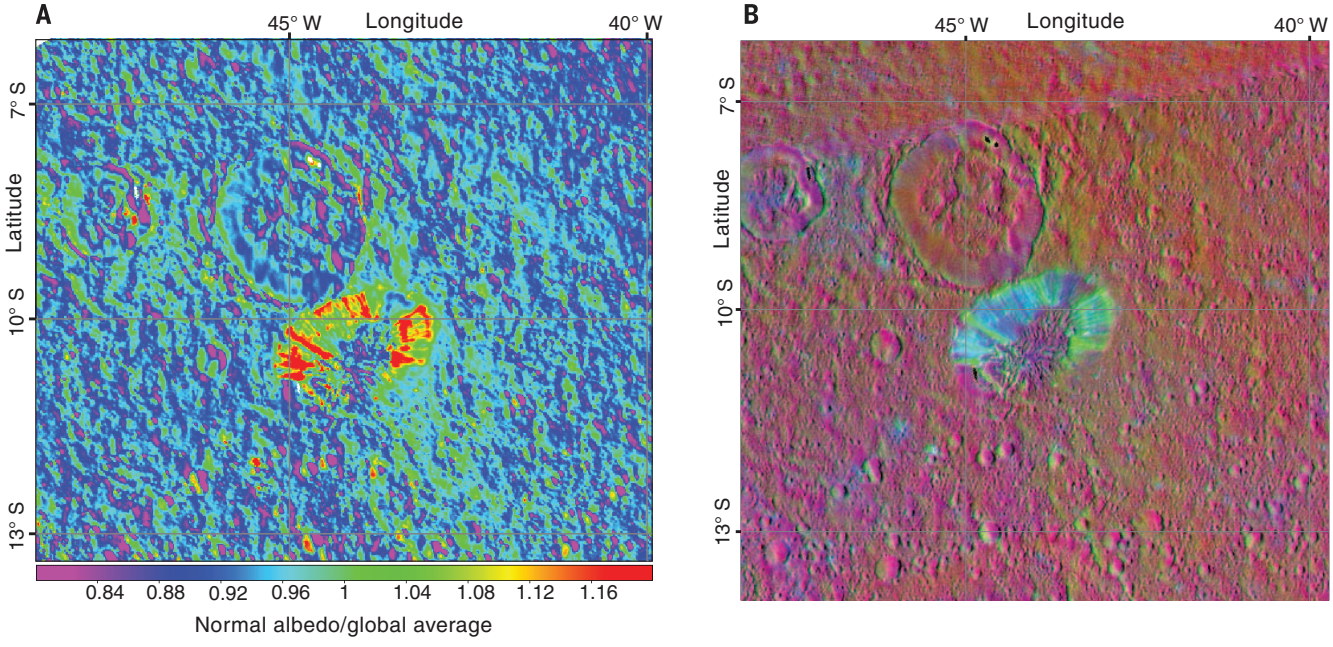

Fig. 4. Albedo map and color composite from FC images. (**A**) Mosaic of ~135 m/pixel, with color code indicating variations relative to the global normal albedo. Ahuna Mons is identified by its high albedo (red color) lineations. Image is ~70 km wide. (**B**) Mosaic of color ratio images [R (red) = 0.97 μm /0.75 μm, G (green) = 0.75 μm, and B (blue) = 0.44 μm /0.75 μm]. Image is ~70 km wide.

the high aspect ratio (edifice height/basal diameter) of Ahuna Mons (~0.24) can be produced by a thin elastic layer (<5 km) and a large density contrast (between diapir and surroundings) of >500 kg m^{-3}. Evidence for a thin elastic crust on Ceres is currently lacking (*1*, *14*), while such a large density contrast would require a high concentration of volatiles within a spatially limited (few tens of km) location. Hence the case for diapiric process and surface upwarping is not supported by existing conditions observed on Ceres.

Description of FC albedo and color mosaic

The Framing Camera is equipped with filters covering the range 0.4 μm to 1.0 μm (*12*) for multi-spectral analyses. We used the global average photometric models of Ceres derived from ~400 m/pixel data (*46*) to correct the local scattering geometry to incidence angle 30°, emission angle 0°, and phase angle 30° and remove the effect of local topography in ~135 m/pixel images (Fig. 4A). The photometrically corrected images from multiple filters were rectified and map projected, and combined to produce false-color mosaic for the Ahuna Mons region. The false-color mosaic was calculated with the following reflectance ratios: red channel shows R(0.97 μm)/R (0.75 μm), green channel shows R(0.75 μm) and blue channel shows R(0.44 μm)/R(0.75 μm), with R the reflectance at the given wavelength (Fig. 4B). These ratios enable the identification of the changes in the visible spectrum of Ceres at global and regional scales. The area surrounding

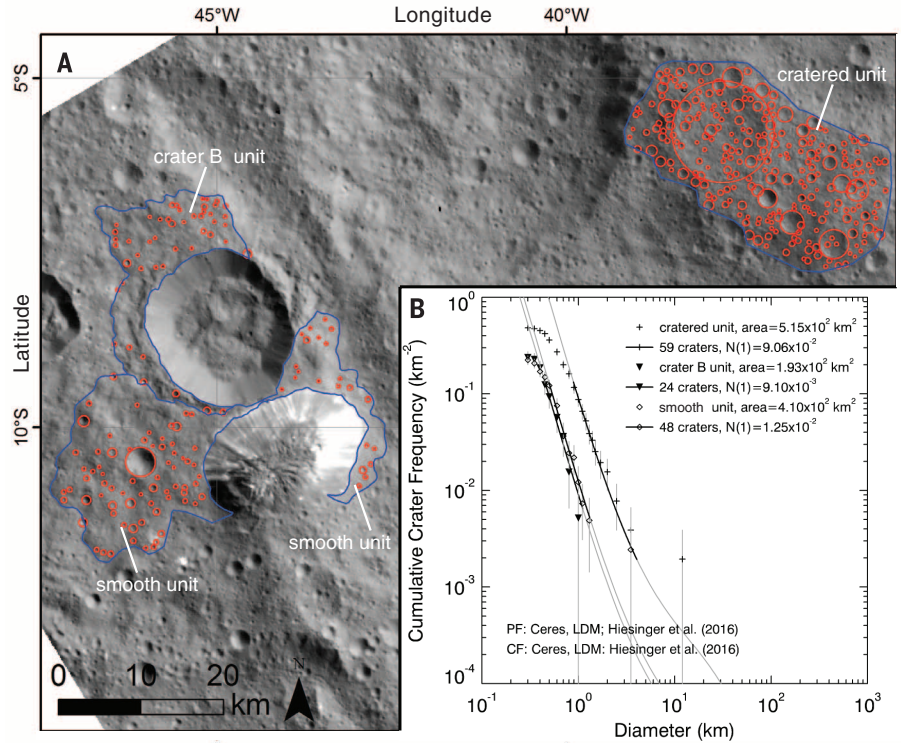

Fig. 5. Crater size-frequency distribution measurements of three areas in the Ahuna Mons region. (**A** and **B**) Two sets of production and chronology functions are applied in order to derive absolute model ages (*14*). (B) The Lunar Derived Model gives the following absolute model ages: cratered unit (crosses), 1.55 ± 0.20 Ga; smooth unit (diamonds), 210 ± 30 Ma; crater B unit (inverted solid triangle), 160 ± 30 Ma. The Asteroid Derived Model gives the following absolute model ages: cratered unit (crosses), ~440 ± 60 million years; smooth unit (diamonds), 70 ± 20 million years; crater B unit (inverted solid triangle), 70 ± 20 million years. The crater size-frequency distribution technique cannot be applied for the talus and summit units because of the slope and overall small surface area. Secondary crater chains (Fig. 1C) heavily affect the surface of the tholus, preventing reliable determination of crater size-frequency distributions for the area.

Ahuna Mons appears reddish punctuated by blue spots, probably small (<1 km) impact craters. The talus unit with downslope lineations has different values, appearing cyan and yellow in Fig. 4B; similar values are found elsewhere on Ceres on morphologically fresh-appearing slopes of impact craters and on bright ejecta rays. Most of the lineations display high albedos, reaching values 15% higher than the global average, and their visible wavelength spectrum possesses a negative (blue) slope relative to surrounding material. The summit unit is distinct from the talus and contains reddish areas similar the surrounding terrain. Aside from the downslope lineations, no other clear correlation is found with the geologic map of Fig. 1D.

Estimation of trough depth and carapace thickness

Accurate estimate of the carapace thickness would require knowledge of the troughs (Fig. 3C) formation mechanism and geometry, which cannot be precisely determined at the resolution of the images and the digital terrain model. As a first order approximation, we consider the troughs as symmetric grabens, and adopt the relationship of (*47*). Symmetric graben formation is a consequence of fracturing and uplifting of a brittle layer by an upward intruding viscous fluid (*47*). The width of the graben has a linear correlation with the thickness of the brittle layer, the thickness to width ratio being 0.89 (*47*). With trough widths in the range ~500 m to ~1 km, the carapace depth is estimated to be in the range 450-890 m. This range represents a lower estimate, however, as other formation scenarios are plausible, such as horst and graben or tilted-blocks systems (*48*). Therefore the carapace can be thicker than the estimated range.

Description of the topographic profiles

The topographic profile used for comparison with the static and dynamic models is calculated as follows. As shown in Fig. 2B, the topographic profile SSE-NNW of the Mons is strongly asymmetric, probably because of the pre-existing tholus topography (*28*). A similar setting is found for the Compton-Belkovich complex on the Moon. The profile shown in Fig. 2C perpendicular to the Fig. 2B profile is oriented along the tholus flank and better represents the unaffected Mons shape. Because the profiles differ, three WSW-ENE profiles are averaged (blue lines in Fig. 2A) and used for model comparison (Fig. 7B). The use of the WSW flank is avoided because it is affected by a terrace.

Description of the static model

The shape of a dome in static equilibrium between the pressurized ductile interior (magma) and the rigid carapace can be described by r, the radial coordinate, z, the vertical coordinate, and ϕ the angular coordinate. These variables are related by the following equations (*28*):

$$\frac{d(\sin\phi)}{dr} + \frac{\sin\phi}{r} = \frac{\rho g}{\sigma t} \quad (1)$$

$$\tan\phi = \frac{dz}{dr} \quad (2)$$

where t and σ are the thickness and tensile strength of the carapace, and ρ is the density of the ductile material. Ceres gravitational acceleration is g (0.28 m s^{-2}, (*1*)). The solution of these equations, i.e., the shape of the dome, is governed by a single dimensionless parameter that incorporates all physical parameters, i.e.,

$$D = 1/h\sqrt{\sigma t/\rho g} \quad (3)$$

with h the pressure head (expressed in m) at the apex of the dome (*28*). For magma density we adopt the outer layer density range of 1680–1950 kg m^{-3}, estimated from Dawn's gravity and shape measurement and considering a two layer model for Ceres' interior (*2*). The carapace thickness is estimated to be in the range of 450-890 m based on the summit troughs width and assuming that they formed as symmetric grabens. Tensile strength is taken between 1×10^6 and 1×10^7 Pa, as of terrestrial high-viscosity magmas such as dacites (*28*). The choice of a different composition, i.e., using tensile strength of water ice, has no effect as this water ice property (*49*) is comparable to that of high-viscosity dacite material.

The model profile is fitted to the measured profile for radial distances from the center up to 6.7 km. The latter value represents the distance beyond which the measured profile is dominated by the constant angle of repose of the talus. The talus angle of repose is calculated in a representative section of the profile between the distances 8-11 km. In this range, the difference between the profile calculated with the angle of repose and the measured profile is less than 100 m. The measured profile deviates from the constant angle of repose profile by more than 100 m at distances less than 6.7 km. A root-mean-square error is calculated between distances 0 and 6.7 km. For matching the model and measured profiles an additional constraint is defined: at distances greater than 6.7 km, the model profile is required to have lower elevations than the measured profile.

The static model with the smallest root mean square (RMS) error (~1.0%) is obtained with D

values of ~5 (Fig. 7A). These values are achieved with a pressure at the dome apex (in excess of the hydrostatic pressure) between 5×10^4 Pa and 2×10^5 Pa, depending on the tensile strength, density and thickness ranges, an order of magnitude lower than viscous dome magma pressures on Earth (*28*).

Description of dynamic model

The dynamic model is described in (*30*) and is an improvement of the gravity current model of Newtonian fluids applied to volcanic domes of (*29*). Newtonian fluid behavior is used for simplicity to approximate the complex lava material bearing melt, crystals and volatiles, and usually behaving as a viscoplastic material (*23*, *50*). The model applied here takes into account the viscosity increase with time, an important effect not fully considered in previous work (*29*). We assume a homogeneous ductile core with a circular basal planform. These two properties represent a simplification of Ahuna Mons, because the composite nature of the dome suggests variations in rheology within the core and the basal planform is approximately elliptical. The equation governing the profile of the dome, i.e., elevation h and radius r as a function of time t, is (*30*):

$$h(r,t) = \frac{4V}{3\pi r_0^2}\frac{1}{\left(1+\frac{\theta}{\tau}\right)^{1/4}}\left[1-\frac{r^2}{r_0^2}\frac{1}{\left(1+\frac{\theta}{\tau}\right)^{1/4}}\right]^{1/3} \quad (4)$$

The volume is defined by the profile of the static model ($V = 6.14 \times 10^{11}$ m^3). Keeping the volume constant means spreading occurs once all material is extruded. This is a further simplification of the process forming Ahuna Mons: a possible co-occurrence of spreading and ongoing material extrusion. The initial radius r_0 is arbitrarily taken between 2–6 km. Using values within this range, the final kinematic viscosity value varies less than 10%. The initial elevation h_0, is defined by the volume and initial radius. τ is a time constant. The transformation variable for the time-dependent viscosity is:

$$\theta(t) = \Gamma\left(1 - e^{-t/\Gamma}\right) \quad (5)$$

and it results from defining the time-dependent viscosity as

$$\nu = \nu_0 e^{t/\Gamma} \quad (6)$$

Γ, the timescale over which the viscosity increases exponentially, is found iteratively with the requirement that the dome front does not advance once the relaxation time is reached. The time constant τ is defined with ν_0, the initial bulk kinematic viscosity, as follows:

$$\tau = \left(\frac{3}{4}\right)^5\left(\frac{\pi}{V}\right)^3\frac{\nu_0\nu_0^8}{g} \quad (7)$$

The relaxation time is estimated by considering that the dome stops spreading after significant cooling. An upper estimate is obtained by considering that cooling is limited by conduction. For a dome of elevation d, the cooling by conduction timescale can be approximated as follows (*51*):

$$t_c \sim \frac{d^2}{\kappa} \quad (8)$$

With k delineating thermal diffusivity. Radiative cooling represents a lower estimate as it assumes that the entire dome remains isothermal (*52*):

$$t_r \sim \frac{\rho c_p d}{\sigma T^3} \quad (9)$$

where ρ and c_p are the density and heat capacity, respectively. T is the temperature during spreading and σ the Stefan-Boltzmann constant. The diffusivity depends on the density, thermal conductivity, heat capacity and temperature of the material (*53*). We consider that the material has a density corresponding to the highest value presented above, i.e., 1950 kg m^{-3} (*2*). Uncertainties due to the choice of this composition are discussed at the end of this section. Because the types, proportions and states of mineral components of the Ahuna Mons material are not known, for this calculation we assume it is composed of silicates (density of 2540 kg m^{-3}) and water ice (920 kg m^{-3}). The following properties are calculated assuming a mixture of silicates and ice of density 1950 kg m^{-3} (*53*). Thermal diffusivity is estimated at ~1.5×10^{-6} m^2 s^{-1} and heat capacity at 1242 J kg^{-1} K^{-1} (*53*). The temperature is set at 230K as it is the highest value found at a depth of >50 km from thermal evolution model of Ceres (*35*). Conductive cooling timescales is 3.1×10^5 years, whereas radiative timescale is 4.2×10^2 years.

The fit between the dynamic model profile and the measured profile is performed as for the static model and is described above. For t = 4.2×10^2 years, the smallest RMS error (1.1%) is obtained with $\Gamma = 1.3 \times 10^2$ years and an initial apparent kinematic viscosity of 2.2×10^{12} m^2 s^{-1}, or an initial apparent dynamic viscosity of 4.3×10^{15} Pa s. For t = 3.1×10^5 years, the smallest RMS error (1.1%) is obtained with $\Gamma = 9.2 \times 10^4$ years and an initial apparent kinematic viscosity of 1.6×10^{15} m^2 s^{-1}, or an initial apparent dynamic viscosity of 3.1×10^{18} Pa s. In summary, initial apparent dynamic viscosity is in the range of 4×10^{15} –3×10^{18} Pa s.

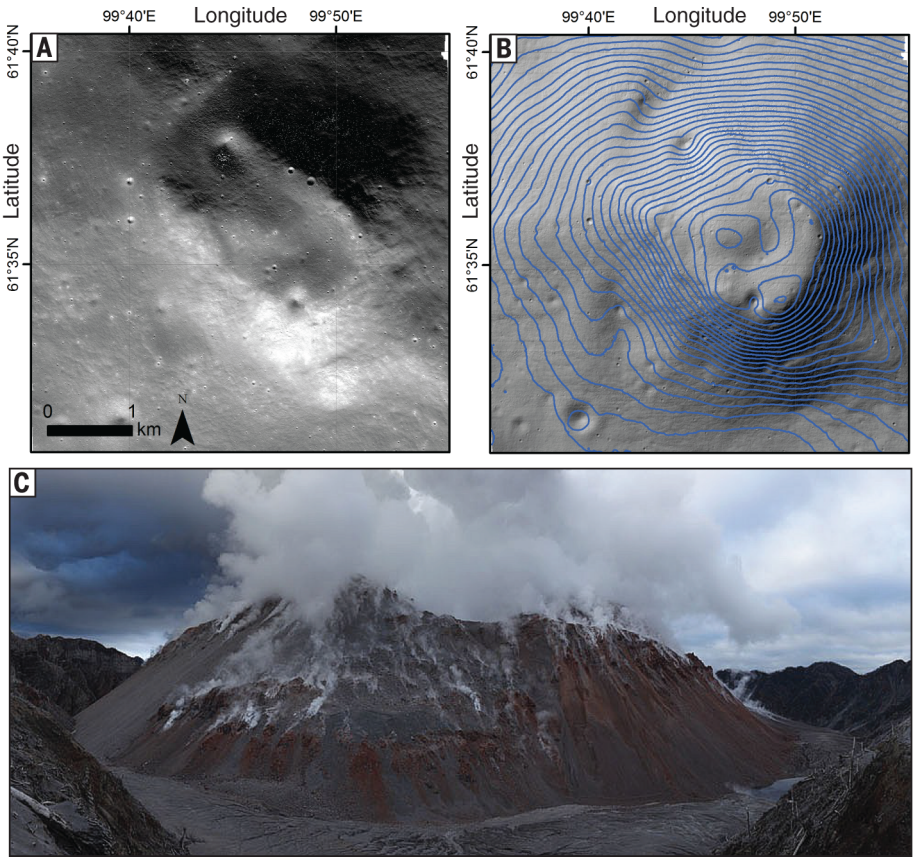

Fig. 6. Lunar and terrestrial analogs. (**A**) Lunar Reconnaissance Orbiter image of the major dome in the Compton-Belkovich volcanic complex on the Moon (*25*). (**B**) Hill-shaded digital terrain model (*27*), with superimposed contour lines in 25-m increments. Same location as (A). The dome has an aspect ratio of ~0.2 (~0.24 for Ahuna Mons) and slopes of ~23° (30° to 40° for Ahuna Mons). An irregular central depression characterizes the summit. (**C**) North view of the Chaitén dome (Chile), where a talus collar with steep slopes is well developed. The dome is 1.7 km in diameter and has an aspect ratio of ~0.2. [Image credit: R. Roscoe]

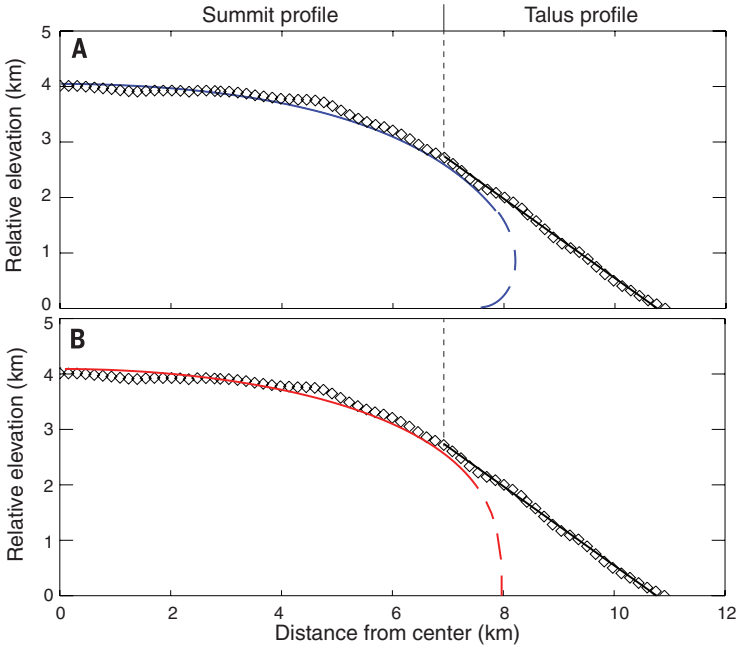

Fig. 7. Topographic profiles of Ahuna Mons and models. (**A**) Average, half topographic profile of Ahuna Mons (from Fig. 2) shown in diamonds, compared with a calculated profile of a static volcanic dome (blue line). The model profile is calculated with carapace tensile strength of 10^7 Pa, thickness of 450 m, and ductile material density of 1680 kg m^{-3}. The blue line is dashed where talus material covers the profile. The constant slope of the talus material is highlighted with a black line (35°). (**B**) Same as (A) but with a calculated profile from a dynamic model of volcanic dome (red line). Key values for the model curve are initial radius of 5.6 km, initial height of 8.2 km, initial actual viscosity of 4×10^{15} Pa s, and a relaxation time of 4×10^2 years. The red line is dashed where talus material covers the profile.

The following timescales and viscosities are obtained if a material of pure water ice at 230 K is considered. Although the material of Ahuna is unlikely to correspond to such composition, the differences from a silicate-dominated material are here considered as an estimate of the uncertainties due to composition. Thermal diffusivity for water ice at 230 K is 1.6×10^{-6} m^2 s^{-1} (*53*), leading to conductive timescale of 2.9×10^5 years. Heat capacity is 1803 J kg^{-1} K^{-1} (*53*), leading to radiative timescale of 2.9×10^2 years. Initial apparent dynamic viscosities are in the range 1.4×10^{15}–1.4×10^{18} Pa s, on the same order of magnitude as for a silicate-dominated mixture of density 1950 kg m^{-3}.

REFERENCES AND NOTES

1. C. T. Russell *et al.*, Dawn arrives at Ceres: Exploration of a small volatile-rich world. *Science* **353**, 1008–1010 (2016).
2. R. S. Park *et al.*, A partially differentiated interior for (1) Ceres deduced from its gravity field and shape. *Nature* 10.1038/nature18955 (2016). doi: 10.1038/nature18955; pmid: 27487219
3. M. C. De Sanctis *et al.*, Ammoniated phyllosilicates with a likely outer Solar System origin on (1) Ceres. *Nature* **528**, 241–244 (2015). doi: 10.1038/nature16172; pmid: 26659184
4. P. O. Hayne, O. Aharonson, Thermal stability of ice on Ceres with rough topography. *J. Geophys. Res.* **120**, E004887 (2015).
5. J. S. Kargel, Brine volcanism and the interior structures of asteroids and icy satellites. *Icarus* **94**, 368–390 (1991). doi: 10.1016/0019-1035(91)90235-L
6. J. S. Kargel, Cryovolcanism on the icy satellites. *Earth Moon Planets* **67**, 101–113 (1994). doi: 10.1007/BF00613296
7. P. M. Schenk, W. B. McKinnon, D. Gwynn, J. M. Moore, Flooding of Ganymede's bright terrains by low-viscosity water-ice lavas. *Nature* **410**, 57–60 (2001). doi: 10.1038/35065027; pmid: 11242037
8. C. C. Porco *et al.*, Cassini observes the active south pole of Enceladus. *Science* **311**, 1393–1401 (2006). doi: 10.1126/science.1123013; pmid: 16527964
9. L. M. Prockter *et al.*, Characteristics of icy surfaces. *Space Sci. Rev.* **153**, 63–111 (2010). doi: 10.1007/s11214-010-9649-8
10. K. Stephan, R. Jaumann, R. Wagner, Geology of icy bodies, in *Science of Solar System ices*, M.S. Gudipati, J. Castillo-Rogez, Eds. (Springer, 2013), pp. 279–370.
11. S. A. Fagents, Considerations for effusive cryovolcanism on Europa: The post-Galileo perspective. *J. Geophys. Res.* **108** (E12), 2139 (2003). doi: 10.1029/2003JE002128
12. H. Sierks *et al.*, The Dawn Framing Camera. *Space Sci. Rev.* **163**, 263–327 (2011). doi: 10.1007/s11214-011-9745-4
13. D. L. Buczkowski *et al.*, The geomorphology of Ceres. *Science* **353**, aaf4332 (2016).
14. H. Hiesinger *et al.*, Cratering on Ceres: Implications for its crust and evolution. *Science* **353**, aaf4759 (2016).
15. O. Merle, A. Borgia, Scaled experiments of volcanic spreading. *J. Geophys. Res.* **101** (B6), 13805–13817 (1996). doi: 10.1029/95JB03736
16. T. Kneissl, S. van Gasselt, G. Neukum, Map-projection-independent crater size-frequency determination in GIS environments—New software tool for ArcGIS. *Planet. Space Sci.* **59**, 1243–1254 (2011). doi: 10.1016/j.pss.2010.03.015
17. G. G. Michael, G. Neukum, Planetary surface dating from crater size-frequency distribution measurements: Partial resurfacing events and statistical age uncertainty. *Earth Planet. Sci. Lett.* **294**, 223–229 (2010). doi: 10.1016/j.epsl.2009.12.041
18. O. Ruesch *et al.*, Geologic map of the northern hemisphere of Vesta based on Dawn Framing Camera (FC) images. *Icarus* **244**, 41–59 (2014). doi: 10.1016/j.icarus.2014.01.035
19. Impact flux on Ceres and Vesta are similar for 1-km craters, but different target properties result in larger crater diameters on Ceres relative to Vesta.
20. J. H. Fink, N. T. Bridges, Effects of eruption history and cooling rate on lava dome growth. *Bull. Volcanol.* **57**, 229–239 (1995). doi: 10.1007/BF00265423
21. M. R. Hudec, M. P. A. Jackson, Terra infirma: Understanding salt tectonics. *Earth Sci. Rev.* **82**, 1–28 (2007). doi: 10.1016/j.earscirev.2007.01.001
22. C. J. Talbot, P. Aftabi, Geology and models of salt extrusion at Qum Kuh, central Iran. *J. Geol. Soc. London* **161**, 321–334 (2004). doi: 10.1144/0016-764903-102
23. S. Blake, Viscoplastic models of lava domes, in *Lava Flows and Domes*, J. H. Fink, Ed. (Springer, 1990), pp. 88–126.
24. S. W. Anderson, J. H. Fink, The development and distribution of surface textures at the Mount St. Helens dome, in *Lava Flows and Domes*, J. H. Fink, Ed. (Springer, 1990), pp. 25–46.
25. A. V. Shevchenko, V. N. Dvigalo, I. Y. Svirid, Airborne photogrammetry and geomorphological analysis of the 2001–2002 exogenous dome growth at Molodoy Shiveluch Volcano, Kamchatka. *J. Volc. Geoth. Res.* **304**, 94–107 (2015). doi: 10.1016/j.jvolgeores.2015.08.013
26. S. W. Anderson, E. R. Stofan, J. J. Plaut, D. A. Crown, Block size distributions on silicic lava flow surfaces: Implications for emplacement conditions. *GSA Bull.* **110**, 1258–1267 (1998). doi: 10.1130/0016-7606(1998)110<1258:BSDOSL>2.3.CO;2
27. B. L. Jolliff *et al.*, Non-mare silicic volcanism on the lunar farside at Compton-Belkovich. *Nat. Geosci.* **4**, 566–571 (2011). doi: 10.1038/ngeo1212
28. R. M. Iverson, Lava domes modeled as brittle shells that enclose pressurized magma, with application to Mount St. Helens, in *Lava Flows and Domes*, J. H. Fink, Ed. (Springer, 1990), pp. 47–69.
29. H. E. Huppert, The propagation of two-dimensional and axisymmetric viscous gravity currents over a rigid horizontal surface. *J. Fluid Mech.* **121**, 43–58 (1982). doi: 10.1017/S0022112082001797
30. L. C. Quick, L. S. Glaze, S. M. Baloga, E. R. Stofan, New approaches to inferences for steep-sided domes on Venus. *J. Volc. Geoth. Res.* **319**, 93–105 (2016). doi: 10.1016/j.jvolgeores.2016.02.028
31. C. R. Manley, Extended cooling and viscous flow of large, hot rhyolite lavas: Implications of numerical modeling results *J. Volc. Geoth. Res.* **53**, 27–46 (1992). doi: 10.1016/0377-0273(92)90072-L
32. A. J. Hale, E. S. Calder, G. Wadge, S. C. Loughlin, G. A. Ryan, Modelling the lava dome extruded at Soufriere Hills Volcano, Montserrat, August 2005-May 2006 part 1: Dome shape and internal structure. *J. Volc. Geoth. Res.* **187**, 53–68 (2009). doi: 10.1016/j.jvolgeores.2009.08.023
33. P. H. Schultz, D. A. Crawford, Origin of nearside structural and geochemical anomalies on the Moon. *GSA Special Papers* **477**, 141–159 (2011).
34. M. C. De Sanctis *et al.*, Bright carbonate deposits as evidence of aqueous alteration on (1) Ceres. *Nature* **536**, 54–57 (2016). doi: 10.1038/nature18290; pmid: 27362221
35. J. C. Castillo-Rogez, T. B. McCord, Ceres' evolution and present state constrained by shape data. *Icarus* **205**, 443–459 (2010). doi: 10.1016/j.icarus.2009.04.008
36. D. W. Davis, T. K. Lowenstein, R. J. Spencer, Melting behavior of fluid inclusions in laboratory-grown halite crystals in the systems NaCl–H_2O, NaCl–KCl–H_2O, NaCl–$MgCl_2$–H_2O, and NaCl–$CaCl_2$–H_2O. *Geo. Cosm. Acta* **54**, 596–601 (1990).
37. M. Arakawa, N. Maeno, Effective viscosity of partially melted ice in the ammonia-water system. *Geophys. Res. Lett.* **21**, 1515–1518 (1994). doi: 10.1029/94GL01041
38. J. C. Castillo-Rogez, J. I. Lunine, Evolution of Titan's rocky core constrained by Cassini observations. *Geophys. Res. Lett.* **37**, L20205 (2010). doi: 10.1029/2010GL044398
39. H. Y. McSween, D. W. Mittlefehldt, A. W. Beck, R. G. Mayne, T. J. McCoy, HED meteorites and their relationship to the geology of Vesta and the Dawn mission. *Space Sci. Rev.* **163**, 141–174 (2011). doi: 10.1007/s11214-010-9637-z
40. R. Jaumann *et al.*, The high-resolution stereo camera (HRSC) experiment on Mars Express: Instrument aspects and experiment conduct from interplanetary cruise through the nominal mission. *Planet. Space Sci.* **55**, 928–952 (2007). doi: 10.1016/j.pss.2006.12.003
41. K. Gwinner *et al.*, Derivation and validation of high-resolution digital terrain models from Mars Express HRSC data. *Photogramm. Eng. Remote Sensing* **75**, 1127–1142 (2009). doi: 10.14358/PERS.75.9.1127
42. F. Preusker *et al.*, Stereo topographic models of Mercury after three MESSENGER flybys. *Planet. Space Sci.* **59**, 1910–1917 (2011). doi: 10.1016/j.pss.2011.07.005
43. R. Jaumann *et al.*, Vesta's shape and morphology. *Science* **336**, 687–690 (2012). doi: 10.1126/science.1219122; pmid: 22582254
44. F. Preusker *et al.*, Shape model, reference system definition, and cartographic mapping standards for comet 67P/Churyumov-Gerasimenko–Stereo-phptogrammetric analysis of

Rosetta/OSIRIS image data. *Astron. Astrophys.* **583**, A33 (2015). doi: 10.1051/0004-6361/201526349
45. A. B. Watts, *Isostasy and Flexure of the Lithosphere* (Cambridge Univ. Press, 2001).
46. J.-Y. Li *et al.*, Surface albedo and spectral variability on Ceres. *Astrophys. J.* **817**, L22 (2016). doi: 10.3847/2041-8205/817/2/L22
47. E. Brothelande, O. Merle, Estimation of magma depth for resurgent domes: An experimental approach. *Earth Planet. Sci. Lett.* **412**, 143–151 (2015). doi: 10.1016/j.epsl.2014.12.011
48. R. T. Pappalardo, R. Greeley, A review of the origins of subparallel ridges and troughs: Generalized morphological predictions from terrestrial models. *J. Geophys. Res.* **100** (E9), 18985–19007 (1995). doi: 10.1029/94JE02638
49. J. J. Petrovic, Review mechanical properties of ice and snow. *J. Mater. Sci.* **38**, 1–6 (2003). doi: 10.1023/A:1021134128038
50. H. J. Melosh, D. M. Janes, Ice volcanism on ariel. *Science* **245**, 195–196 (1989). doi: 10.1126/science.245.4914.195-a; pmid: 17787879
51. D. L. Turcotte, G. Schubert, *Geodynamics* (Cambridge Univ. Press, ed. 3, 2014).
52. J. Crisp, S. Baloga, A model for lava flows with two thermal components. *J. Geophys. Res.* **95** (B2), 1255–1270 (1990). doi: 10.1029/JB095iB02p01255
53. T. B. McCord, C. Sotin, Ceres: Evolution and current state. *J. Geophys. Res.* **110** (E5), E05009 (2005). doi: 10.1029/2004JE002244

ACKNOWLEDGMENTS

The Framing Camera system on the spacecraft was developed and built under the leadership of the Max Planck Institute for Solar System Research in Göttingen, Germany, in collaboration with the DLR Institute of Planetary Research in Berlin and the Institute of Computer and Communication Network Engineering in Braunschweig. The Framing Camera project is funded by the Max Planck Society, DLR, and NASA/Jet Propulsion Laboratory. The Dawn spacecraft Operations and Flight teams made the observations possible and are acknowledged for their efforts. O.R. is supported by an appointment to the NASA Postdoctoral Program at the NASA Goddard Space Flight Center administered by Universities Space Research Association through a contract with NASA. N.S., A.Ne., and J.H.P. acknowledge partial support by DLR. M.T.B. acknowledges support by the NASA Dawn at Ceres Guest Investigator Program Award NNH15AZ85I. We acknowledge the careful and highly beneficial reviews by anonymous referees. Dawn Framing Camera data are archived with the NASA Planetary Data System at http://sbn.psi.edu/pds/resource/dwncfc2.html. O.R. conceived the study, performed the geologic and modeling analyses, and wrote the manuscript. T.P., L.C.Q., D.P.O., S.B., and M.T.B. contributed to the geologic or modeling analyses. J.-Y.L., M.S., A.Na., T.R., M.H., and T.P. contributed with FC data products, and P.S. and F.P. contributed with digital terrain models. N.S., D.P.O., H.H., T.K., A.Ne., and J.H.P. provided absolute model ages. L.A.M., J.C.C.-R., D.A.W., B.E.S., D.L.B., and M.V.S. contributed to the interpretation of the data and its clear communication. C.A.R. and C.T.R. lead the Dawn mission. All authors contributed to the discussion of the results.

5 February 2016; accepted 20 July 2016
10.1126/science.aaf4286

Cryovolcanism on Ceres
O. Ruesch, T. Platz, P. Schenk, L. A. McFadden, J. C. Castillo-Rogez, L. C. Quick, S. Byrne, F. Preusker, D. P. O'Brien, N. Schmedemann, D. A. Williams, J.-Y. Li, M. T. Bland, H. Hiesinger, T. Kneissl, A. Neesemann, M. Schaefer, J. H. Pasckert, B. E. Schmidt, D. L. Buczkowski, M. V. Sykes, A. Nathues, T. Roatsch, M. Hoffmann, C. A. Raymond and C. T. Russell
(September 1, 2016)
Science **353** (6303), . [doi: 10.1126/science.aaf4286]

Editor's Summary

Science (print ISSN 0036-8075; online ISSN 1095-9203) is published weekly, except the last week in December, by the American Association for the Advancement of Science, 1200 New York Avenue NW, Washington, DC 20005.